
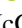






Impact of strong magnetization in cylindrical plasma implosions with applied B-field measured via x-ray emission spectroscopy

M. Bailly-Grandvaux ^{1,*}, R. Florido ², C. A. Walsh,³ G. Pérez-Callejo,⁴ F. N. Beg,¹ P. Bradford,⁵ M. A. Gigosos ⁴, R. C. Mancini,⁶ C. McGuffey,⁷ F. Suzuki-Vidal ⁸, C. Vlachos ⁵ and J. J. Santos ^{5,†}

¹Center for Energy Research, University of California-San Diego, La Jolla, California 92093, USA

²iUNAT-Departamento de Física, Universidad de Las Palmas de Gran Canaria, E-35017 Las Palmas de Gran Canaria, Spain

³Lawrence Livermore National Laboratory, Livermore, California 94550, USA

⁴Departamento de Física Teórica Atómica y Óptica, Universidad de Valladolid, E-47011 Valladolid, Spain

⁵Centre Lasers Intenses et Applications (CELIA), Université de Bordeaux-CNRS-CEA, UMR 5107, F-33405 Talence, France

⁶Physics Department, University of Nevada, Reno, Nevada 89557, USA

⁷General Atomics, San Diego, California 92121, USA

⁸Blackett Laboratory, Imperial College London, London SW7 2AZ, United Kingdom



(Received 31 May 2023; revised 28 September 2023; accepted 8 December 2023; published 19 January 2024)

Magnetization is a key strategy for enhancing inertial fusion performance, though accurate characterization of magnetized dense plasmas is needed for a better comprehension of the underlying physics. Measured spectra from imploding Ar-doped D₂-filled cylinders at the OMEGA laser show distinctive features with and without an imposed magnetic field. A multizone spectroscopic diagnosis leads to quantitative estimates of the plasma conditions, namely revealing a 50% core temperature rise at half mass density when a 30-T seed field is applied. Concurrently, experimental spectra align well with predictions from extended-magnetohydrodynamics simulations, providing strong evidence that the attained core conditions at peak compression are consistent with the impact of a 10-kT compressed field. These results pave the way for the validation of magnetized transport models in dense plasmas and for future magnetized laser implosion experiments at a larger scale.

DOI: [10.1103/PhysRevResearch.6.L012018](https://doi.org/10.1103/PhysRevResearch.6.L012018)

The pursuit of controlled fusion in the laboratory is one of the most visible challenges in high-energy-density (HED) plasma science. The National Ignition Facility (NIF) focused global attention by achieving scientific fusion breakeven on 5 December 2022, with a record 3.15 MJ fusion yield out of 2.05 MJ of input laser energy (target gain ≈ 1.5) [1]. While this is a critical milestone, target gains > 100 will ultimately be required to harness inertial fusion energy for power generation [2].

In the magnetoinertial fusion (MIF) concept, an initial (seed) magnetic field (B-field) is amplified with the compressing target as a result of magnetic flux conservation [3,4]. Magnetized implosions have the potential to achieve higher fusion gains than conventional inertial confinement fusion (ICF), through enhanced α -particle confinement [5–8] and suppression of electron thermal conduction losses perpendicular to the direction of the B-field [9,10]. It can also improve the stability of the implosion, by mitigating Rayleigh-Taylor

hydrodynamic instabilities [11,12] and by relaxing constraints on implosion velocities required to reach ignition conditions.

One caveat in magnetized spherical implosions is that the B-field cannot be everywhere aligned perpendicularly to the compression direction, which leads to a theoretical maximum 40% enhancement of core temperature from magnetization [13,14], as well as implosion asymmetries [15–17]. In contrast, in cylindrical implosions, the magnetic field direction can be conveniently aligned along the target axis while it is being radially compressed [18,19], hence no such limit exists and magnetization effects are easier to probe. Moreover, the underlying physics of B-field compression and magnetized heat transport is easier to model in this geometry, which allows magnetohydrodynamics (MHD) codes to be more easily tested [10]. A laser-driven cylindrical implosion platform has been developed at the OMEGA laser facility [20–23] providing a test bed for MIF-relevant experiments [23,24] and paving the way to the first experimental validations of magnetized transport models in dense plasmas [13].

An accurate diagnosis of plasma conditions is paramount for such model validation and understanding of underlying physics. In most implosion experiments, the electron temperature T_e is inferred from the slope of the bremsstrahlung spectrum [25], and the ion temperature T_i from neutron time-of-flight (nTOF) detectors [26]. Density is then deduced from T_i , either assuming a uniform hot spot or invoking an isobaric compression model [14]. However, neutron spectral measurements are susceptible to plasma flows and drive/target

*mbaillyg@ucsd.edu

†joao.santos@u-bordeaux.fr

imperfections, resulting in large experimental fluctuations hindering data inference [27,28]. This is evidenced in a similar configuration as the work presented here, in Ref. [23], where the neutron-average ion temperature of repeated unmagnetized shots was comparable to the change observed between unmagnetized and magnetized shots.

Seeking a more robust method to diagnose magnetization changes in the imploding plasmas, we added a dopant into the fuel to extract electron temperature and density information encoded in its x-ray line emission spectrum. While this is a well-established technique in unmagnetized scenarios, e.g. Refs. [27,29–33], and more recently in the magnetized liner inertial fusion (MagLIF) context [34–36], to the best of our knowledge, it is yet to be used to diagnose strong magnetization in laser-driven implosions.

In this Letter, we report a consistent record 50% increase in the temperature of the core and a $\sim 2\times$ decrease in the core density achieved through cylindrical implosion experiments carried out at the OMEGA laser facility when a 30-T seed B-field is applied. Magnetization effects in cylindrical implosions are reproducibly demonstrated from the systematic changes in K -shell emission lines from the Ar dopant added to the fuel (while neutron measurements were inconclusive). The results were obtained using a multizone spectroscopic model and random χ^2 -minimization analysis of the entire Ar-dopant K -shell emission spectra with and without an applied seed B-field. As such, the present work provides a decisive step towards using advanced spectroscopy techniques in implosion experiments to benchmark models of magnetized transport in dense plasmas—an idea first outlined in Ref. [10]. We will show that, at similar convergence, the experimental data with and without applied B-field align well with the predictions from two-dimensional (2D) extended-MHD simulations, indicating that the observed differences in temperature and density are effectively induced by the seed B-field being compressed to ~ 10 kT.

A schematic of the experimental setup is shown in Fig. 1. The targets are 2.5-mm-long cylinders, with an outer diameter of 600 μm , enclosed by a 19- μm -thick plastic shell. Targets are filled with D_2 gas at 11 atm (1.81 mg/cm^3) and doped with 0.13 at. % of argon. They were symmetrically imploded using a 40-beam, 14.5-kJ laser drive, with a 1.5-ns square pulse (rise and fall times of ~ 100 ps) at a laser wavelength $\lambda = 351$ nm. The laser beams form a quasiuniform irradiation pattern at an intensity of ~ 700 TW/cm^2 over a ~ 0.7 mm cylinder length. The implosions are magnetized using the Magneto Inertial Fusion Electrical Discharge System (MIFEDS) electromagnet [37], delivering a seed B-field of 30 T along the axis of the targets. X-ray framing cameras (XRFCs) were used to track the implosion trajectory, while an x-ray flat crystal spectrometer (XRS) [38] collected the K -shell line spectra from the argon tracer to diagnose the conditions of the compressed core.

The experiments were modeled using the 2D extended-MHD code GORGON [16,39–41], with the setup of the MHD simulations discussed in Ref. [10]. Figure 2(a) shows the experimental values for the radius of the compressed core near maximum compression for both the 0 T (blue) and 30 T case (red) together with the predictions from 2D extended-MHD simulations (solid lines). The experimental core radius is defined as the half width at half maximum of

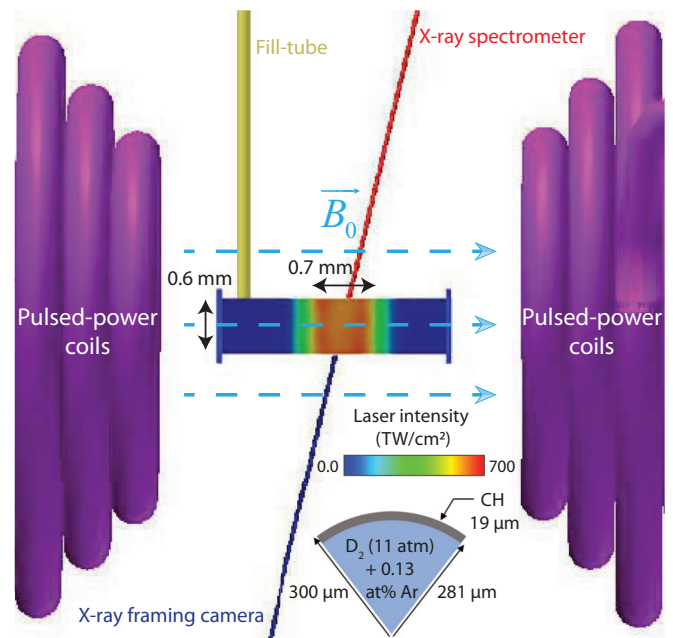


FIG. 1. Schematic of the experimental setup. The color scale on the cylinder corresponds to the laser intensity. The two pulsed-power coils were assembled in a Helmholtz-like configuration, producing a seed B-field of 30 T along the cylinder axis. The fill tube and lines of sight to the main diagnostics (x-ray framing camera and spectrometer) are also shown. The inset gives the geometrical details and composition of the gas-filled cylinders.

the fuel emission in the XRFC images [see Fig. 2(a) inset]. The predicted core radius is obtained by a convolution of the D_2 fuel radius in the simulations with the instrument response, in order to compare the same *apparent radius* between experiment and simulations [42].

At maximum compression, the measured core radius was for both with and without applied B-field ~ 12 – 15 μm , while the simulations predict a minimum apparent radius of ~ 8 – 10 μm . This is a common discrepancy in this type of experiments, since in 2D cylindrical simulations, the laser irradiation is averaged along the azimuthal direction, and therefore drive asymmetries are not fully captured. Such drive asymmetries result in the growth of hydrodynamic instabilities which can become comparable in size to the small hot spots obtained here near maximum compression [24,43]. Even when fully including drive asymmetries in 3D simulations, it is found that other experimental variations can distort the implosion and reduce hot-spot confinement [44].

Notwithstanding, our simulations accurately reproduce the radial evolution of the compressed core up to 1.45 ns after the onset of the laser pulse [42], when peak compression is observed in the experiment (i.e., when the simulated core radius matches the value of ~ 12 μm measured at peak compression with XRFC). Figure 2(b) shows the temperature (left) and density (right) of the cylinder at $t = 1.45$ ns for the magnetized (top) and unmagnetized (bottom) simulations. At this time, the seed B-field is already compressed to 10 kT, significantly altering the hydrodynamic conditions of the fuel. The compressed B-field's effects are evident in both the temperature increase (due to reduced energy losses) and the

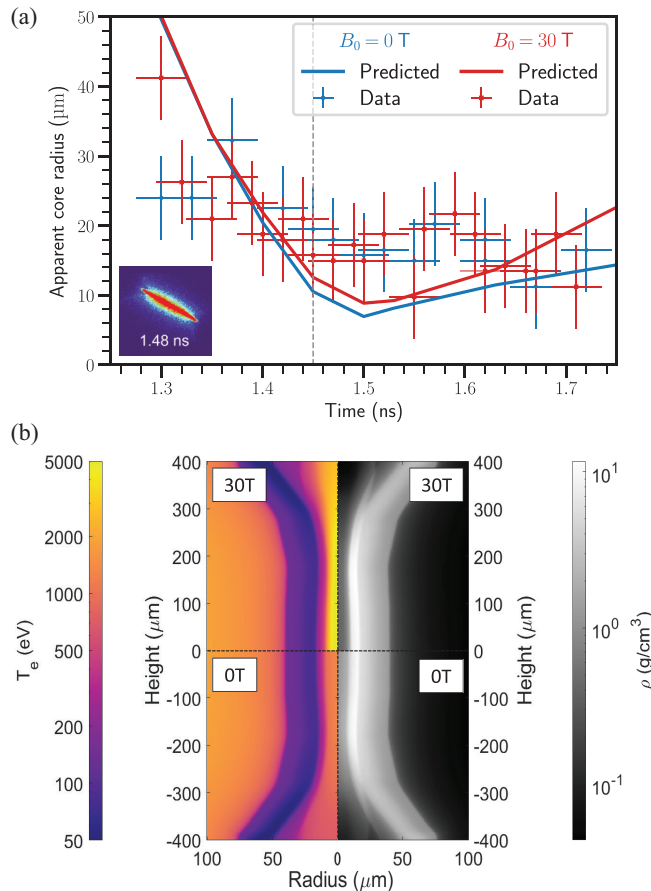


FIG. 2. (a) Core radius near maximum compression, measured from the XRFC. The solid lines correspond to the core radius predicted from the 2D extended-MHD simulations. The inset shows an example image from the XRFC, taken at $t \sim 1.45$ ns. (b) Temperature (left) and density (right) of the plasma for $B_0 = 30$ T (top) and $B_0 = 0$ T (bottom) extracted from the 2D extended-MHD simulations at $t = 1.45$ ns, when the simulated core radius is closest to the experimental value of $r \sim 12$ μm at maximum compression.

decrease in the core density (owing to the effect of magnetic pressure) [10].

The space- and time-integrated Ar emission spectra collected in the experiment and averaged over four magnetized shots ($B_0 = 30$ T) and two unmagnetized shots ($B_0 = 0$) are shown in Figs. 3(a) and 3(b), respectively. A total of six main line transitions in two different charge states are observed, i.e., $\text{He}\alpha$ ($1s2p \rightarrow 1s^2$), $\text{He}\beta$ ($1s3p \rightarrow 1s^2$), and $\text{He}\gamma$ ($1s4p \rightarrow 1s^2$) in He-like Ar, and $\text{Ly}\alpha$ ($2p \rightarrow 1s$), $\text{Ly}\beta$ ($3p \rightarrow 1s$), and $\text{Ly}\gamma$ ($4p \rightarrow 1s$) in H-like Ar. Weaker, and sometimes heavily blended with the parent line, satellite lines arising from autoionizing states in He- and Li-like Ar are also present in the data. The $\text{He}\alpha$ line has been excluded in the 0-T case, since the spectrometer presented a shielding defect for those shots, resulting in a spot of parasitic light that obscured the $\text{He}\alpha$ region. Remarkably, the spectra in both cases were highly reproducible, exhibiting an almost perfect overlap for repeated shots, as shown by the min/max band in the plots. Furthermore, systematic differences in the spectra are evident between unmagnetized and magnetized cases. In the

magnetized scenario, the ratios of H-like to He-like Ar line intensities are notably higher, indicating an increase in the population of H-like Ar ions, which suggests a hotter core for the magnetized implosions.

To measure the imploding core conditions in both magnetized and unmagnetized cases, we performed an independent spectroscopic analysis, requiring no inputs from MHD simulations or implosion models for spatial profiles of core temperature and density. Experimental spectra were fitted using a multizone spectroscopic model, which accounted for possible radial gradients in the plasma conditions and radiation transport effects along the diagnostic line of sight. Raw data were corrected for frequency-dependent Be filter attenuation, crystal reflectivity, x-ray film response, and continuum emission subtraction before model comparison. The required atomic level population distributions, emissivities, and opacities were calculated with the collisional radiative model ABAKO [45] and state-of-the-art Stark-broadened line shapes were provided either by the computer simulation code SIMULA [46,47] or MODELA—a numerically improved version of the standard Stark-broadening theory [48,49]—for the main and satellite transitions, respectively. The frequency-dependent attenuation of the line emission due to shell opacity was also taken into account [31,32]. The instrument resolution was reproduced by a convolution with a Gaussian filter of the appropriate width.

A random-search χ^2 minimization was then performed over a comprehensive database of frequency-dependent emissivities and opacities calculated across a wide range of density and temperature conditions. To constrain the model search, in alignment with implosion physics, we made the fundamental assumption of a monotonic increase/decrease in core density/temperature with radius. We set the number of radial zones to six, which we found to be an optimal value between the computational cost of the minimization procedure and the need to capture sufficient spatial structure for a reliable fit to the data. The only user input required for this analysis was the core radius, set to 15 μm based on our XRFC results. Importantly, we found that the averaged conditions extracted from the fit remained effectively independent of the chosen core radius (within the uncertainties given by the XRFC data), which supports the robustness of the results.

Figure 3 also presents the best-fitting spectra (black dashed lines) and the corresponding intensity contributions from different radial zones of the core (colored dashed lines) along the line of sight—with *zone 1* the innermost zone and *zone 6* the outermost one. These are compared to the mean experimental spectrum for the magnetized case and the unmagnetized case. As expected, we note that He-like lines are dominated by the contribution from outer (colder) zones, while H-like lines emerge from deeper (hotter) zones inside the core. The contribution from zones 1 and 2 is minimal in the magnetized case, indicating a high temperature (>2.5 keV) at the core center, where Ar would be almost fully ionized, resulting in the loss of line emission.

Our model tends to underestimate the emission of satellite lines, with the most noticeable discrepancy occurring in the case of He-like satellites to $\text{Ly}\alpha$. This disagreement could, in principle, be attributed to unaccounted nonuniformities of the core conditions along the cylinder axis and the relatively

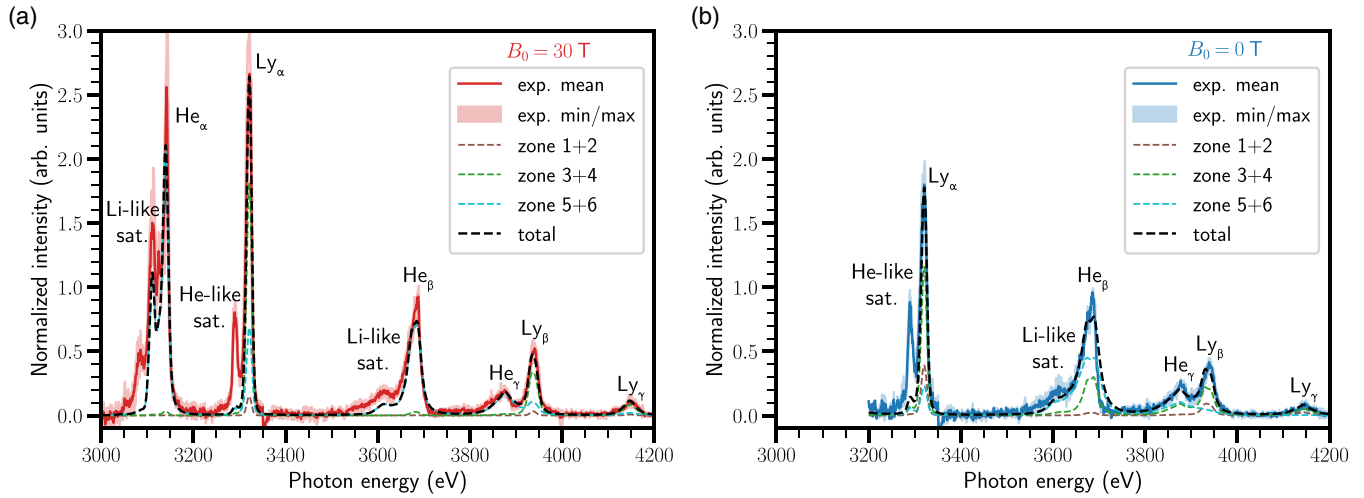


FIG. 3. Time-integrated Ar K -shell spectra for $B_0 = 30$ T [red in (a)] and $B_0 = 0$ [blue in (b)], normalized to the peak of the $\text{He}\beta$. Narrow min/max error bands demonstrate high data reproducibility. Multizone spectroscopic model fits are shown on top, with the total spectra as the black dashed line, and the contribution from different radial zones marked as a dotted colored line. Raw data were postprocessed to correct for the instrument response and continuum emission.

intricate modeling of the autoionization and electron capture balances that impact the population kinetics of autoionizing states.

Remarkably, by combining the multizone spectroscopic model with random χ^2 minimization, we successfully match up to six primary line transitions spanning from states with principal quantum numbers $n = 2, 3, 4$ to $n = 1$ in two different charge states. Moreover, in contrast to the conventional approach of inferring density from one single line shape (typically $\text{He}\beta$) and temperature from measurements of one or two line intensity ratios, e.g., Refs. [24,27,29,50,51], our methodology relies on the whole apparatus of non-Local Thermal Equilibrium (non-LTE) atomic kinetics, Stark-broadening theory, and radiation transport to fit the entire recorded spectra. In both the magnetized and unmagnetized cases, our model satisfactorily reproduces the experimental relative intensity distributions as well as the Stark- and opacity-broadened profiles of the referred lines, which suffices to capture the temperature and density dependence. This robustly supports the reliability of the method [52].

Our integrated approach allows us to simultaneously determine the intensity-averaged temperature and density of the imploding core, leading to the following values for each case,

$$\begin{aligned} T_e^{0T} &= 1000 \pm 30 \text{ eV}, & \rho^{0T} &= 3.22 \pm 0.16 \text{ g/cm}^3, \\ T_e^{30T} &= 1476 \pm 127 \text{ eV}, & \rho^{30T} &= 1.49 \pm 0.11 \text{ g/cm}^3, \end{aligned}$$

with the uncertainties calculated as the corresponding standard deviations over multiple runs of the minimization procedure. These results clearly indicate a hotter and less dense core around stagnation for the implosions where a seed B-field was applied, with the temperature increasing $50 \pm 20\%$ and the density decreasing by a factor of 2.2 ± 0.3 .

To understand the origin of these temperature and density differences, we postprocessed the MHD simulation output to produce synthetic spectra. The calculation procedure is conceptually identical to the one followed in the spectroscopic model used for diagnosis, with the only difference that now

the core temperature and density spatial profiles are those produced by the simulation at every time step (with a maximum resolution of 10 ps near maximum compression).

In Fig. 4, we show the comparison between experimental and synthetic spectra for both the case with a 30-T seed B-field [Fig. 4(a)] and the case with no applied B-field [Fig. 4(b)]. The synthetic spectra are time integrated from simulation outputs until 1.45–1.48 ns, matching experimental peak compression. A good agreement is found between the synthetic and experimental spectra. Interestingly, the respective core-averaged temperature and density predicted at these times are similar to the values inferred from the previous quantitative spectroscopic analysis. Including times closer to 1.5 ns resulted in large discrepancies, which confirms the overestimation of peak compression in MHD simulations. Furthermore, integrating spectra beyond peak compression ($t > 1.5$ ns) induced minor changes in the synthetic spectra that did not improve the comparison with experimental data. This suggests a rapid decrease in the emission after experimental peak compression, likely due to the ensuing onset of hydrodynamic instabilities and mix [24,43,44].

The agreement between synthetic and experimental spectra firmly indicates that the differences in the temperature and density conditions obtained in the magnetized case are caused by the ~ 10 -kT compressed B-field predicted in the simulation. Upon this validation, we can calculate volume-averaged metrics of the core magnetization, which can be directly compared with other magnetized implosion experiments. The plasma magnetization caused by the compressed B-field can be quantified microscopically using the dimensionless Hall parameter, $\omega_{c,e}\tau_{e,i}$, where $\omega_{c,e} = eB/m_e$ is the electron gyrofrequency and $\tau_{e,i}$ is the electron-ion collision timescale ($\propto T_e^{3/2}/n_e$). Physically, the Hall parameter corresponds to the average number of electron gyrations around the B-field lines before colliding with an ion. Therefore, it indicates the role of the B-field on electron energy transport. Here, the Hall parameter calculated from volume-averaged core conditions at $t = 1.45$ ns in simulation (Fig. 2) has a

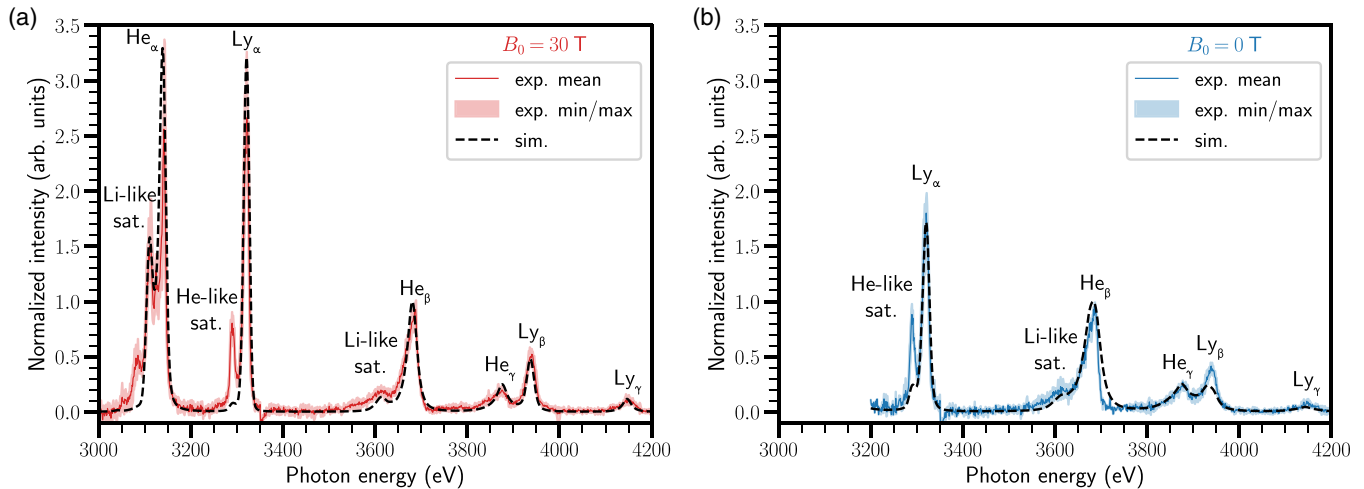


FIG. 4. Time-integrated Ar K -shell spectra shown following the color convention in Fig. 3. The black dashed curves are the time-integrated synthetic spectra postprocessed from the 2D extended-MHD simulations, as described in the text. Good agreement is obtained between experimental and synthetic spectra for the two cases.

large value of ~ 85 , suppressing heat losses [9,10] along the radial direction and leading to a higher core temperature. On the other hand, we can quantify the macroscopic effect of the magnetic pressure $p_{\text{mag}} = B^2/2\mu_0$ on hydrodynamics by comparing it to the total plasma thermal pressure (electrons and ions) p_{th} , which defines the plasma $\beta = p_{\text{th}}/p_{\text{mag}}$ parameter. For the values obtained in this work, the plasma β calculated from volume-averaged core conditions is ~ 8 , which means that the magnetic pressure is not negligible and can reduce core compressibility, resulting in the lower final density observed in the magnetized case compared to the unmagnetized case.

The convergence ratio (CR), which is defined as the initial target radius divided by the final target radius, is CR 20-25. In the limit that the B-field is frozen with the plasma motion (frozen in flow), it would correspond to a compressed B-field of $B_0\text{CR}^2 \sim 12\text{--}18$ kT. To evaluate B-field compressibility, one can calculate a frozen-in-flow factor (see Ref. [10]), defined as $\Gamma = B\rho_0/B_0\rho$, where B , ρ and B_0 , ρ_0 are respectively the final and initial volume-averaged B-field strengths and fuel mass densities. We find $\Gamma \sim 0.65$, meaning that $\sim 35\%$ of the magnetic flux has been lost from the hot spot, a value that is close to what has been reported in previous work [53]. The losses are likely due to axial plasma motion here since diffusion is low (large magnetic Reynolds number) and the Nernst effect is expected to be largely suppressed due to the high magnetization [10].

The results presented in this Letter demonstrate the suitability of dopant spectroscopy as a reliable technique to unravel the effects of high magnetization in plasma conditions. Here, the technique is applied to discern the effects of magnetization in cylindrical implosions. The spectroscopic analysis allows us to build a bridge with the underlying physics of extended MHD, as the results align well with the impact of the predicted ~ 10 kT compressed magnetic field in suppressing radial heat conduction. This leads to a 50% mass-averaged core temperature increase from 1 to ~ 1.5 keV, and to a decrease of the core density by a factor ~ 2 due to the magnetic pressure effect.

The prospects of this diagnostic approach for the study of plasma magnetization are significant, warranting detailed time- and spatially resolved electron temperature measurements. Future work also includes expanding the range of applicability of this spectroscopic technique by adding traces of krypton to the gas mix. Argon ions become nearly fully ionized at electron temperatures > 2.5 keV, resulting in a reduced sensitivity of Ar K -shell spectroscopy to the hotter region of the core. The addition of Kr would be helpful to probe regions of the core with temperatures exceeding 2.5 keV. The transition from Ar to Kr emission is particularly appealing to diagnose magnetized implosions, where the temperature gradient in the core is steep, with a temperature at the periphery < 2.5 keV and a temperature at the center > 2.5 keV. The combination of Ar and Kr emission spectra with such an effective spatial resolution would thus strongly aid in the reconstruction of the core temperature profiles from spectroscopy measurements, a technique discussed in Ref. [54], where the design of magnetized cylindrical implosions on the Laser Mega Joule (with 20 times more energy in the laser drive) is also presented.

Finally, the steep temperature gradients and the strong magnetic pressure obtained in magnetized implosions can lead to a multitude of extended-MHD effects that affect the compressed magnetic field and the structure of the magnetized core [10]. At high densities, these effects remain to be validated by experimental data, and this platform paves the way for such studies.

We thank the team at General Atomics (GA) and Laboratory for Laser Energetics (LLE) for their excellent work on target fabrication and assembly, as well as the outstanding support from LLE to prepare and execute the experiments on the OMEGA laser facility. C.A.W. acknowledges funding from the U.S. Department of Energy by Lawrence Livermore National Laboratory under Contract No. DE-AC52-07NA27344. F.S.-V. acknowledges funding from the Royal Society (U.K.) through a University Research Fellowship. C.V. acknowledges the support from the LIGHT

S&T Graduate Program (PIA3 Investment for the Future Program, Grant No. ANR-17-EURE-0027). This work is supported by the U.S. National Nuclear Security Administration and National Laser Users' Facility under Award No. DE-NA0003940 and by the U.S. Department of Energy - Office of Science, under Grant No. DE-SC0022250. This work has also been carried out within the framework of the EUROfusion consortium, funded by the European Union via the Euratom Research and Training Program (Grants Agreement No. 633053 and No. 101052200–EUROfusion). The involved

teams have operated within the framework of the Enabling Research Projects: Grants No. AWP17-ENR-IFE-CEA-02 and No. AWP21-ENR-IFE.01.CEA. This research was funded, in part, by the French Agence Nationale de la Recherche (ANR), Project No. ANR-22-CE30-0044. Finally, this work has also been supported by the Research Grants No. PID2019-108764RB-I00 and No. PID2022-137632OB-I00 from the Spanish Ministry of Science and Innovation and by the French State within the framework of the Investment for the Future Program, IdEx, Université de Bordeaux/GPR LIGHT.

-
- [1] A. B. Zylstra *et al.*, Experimental achievement and signatures of ignition at the National Ignition Facility, *Phys. Rev. E* **106**, 025202 (2022).
- [2] M. Dunne *et al.*, Timely delivery of laser inertial fusion energy (LIFE), *Fus. Sci. Technol.* **60**, 19 (2011).
- [3] O. V. Gotchev, J. P. Knauer, P. Y. Chang, N. W. Jang, M. J. Shoup, D. D. Meyerhofer, and R. Betti, Seeding magnetic fields for laser-driven flux compression in high-energy-density plasmas, *Rev. Sci. Instrum.* **80**, 043504 (2009).
- [4] J. P. Knauer, O. V. Gotchev, P. Y. Chang, D. D. Meyerhofer, O. Polomarov, R. Betti, J. A. Frenje, C. K. Li, M. J. E. Manuel, R. D. Petrasso *et al.*, Compressing magnetic fields with high-energy lasers, *Phys. Plasmas* **17**, 056318 (2010).
- [5] P. Y. Chang, G. Fiksel, M. Hohenberger, J. P. Knauer, R. Betti, F. J. Marshall, D. D. Meyerhofer, F. H. Séguin, and R. D. Petrasso, Fusion yield enhancement in magnetized laser-driven implosions, *Phys. Rev. Lett.* **107**, 035006 (2011).
- [6] L. J. Perkins, B. G. Logan, G. B. Zimmerman, and C. J. Werner, Two-dimensional simulations of thermonuclear burn in ignition-scale inertial confinement fusion targets under compressed axial magnetic fields, *Phys. Plasmas* **20**, 072708 (2013).
- [7] L. J. Perkins, D. D. M. Ho, B. G. Logan, G. B. Zimmerman, M. A. Rhodes, D. J. Strozzi, D. T. Blackfield, and S. A. Hawkins, The potential of imposed magnetic fields for enhancing ignition probability and fusion energy yield in indirect-drive inertial confinement fusion, *Phys. Plasmas* **24**, 062708 (2017).
- [8] J. D. Moody, Boosting inertial-confinement-fusion yield with magnetized fuel, *Phys. Online J.* **14**, 51 (2021).
- [9] T. Asahina, H. Nagatomo, A. Sunahara, T. Johzaki, M. Hata, K. Mima, and Y. Sentoku, Validation of thermal conductivity in magnetized plasmas using particle-in-cell simulations, *Phys. Plasmas* **24**, 042117 (2017).
- [10] C. A. Walsh, R. Florido, M. Bailly-Grandvaux, F. Suzuki-Vidal, J. P. Chittenden, A. J. Crilly, M. A. Gigosos, R. C. Mancini, G. Pérez-Callejo, C. Vlachos *et al.*, Exploring extreme magnetization phenomena in directly driven imploding cylindrical targets, *Plasma Phys. Controlled Fusion* **64**, 025007 (2022).
- [11] T. Sano, T. Inoue, and K. Nishihara, Critical magnetic field strength for suppression of the Richtmyer-Meshkov instability in plasmas, *Phys. Rev. Lett.* **111**, 025001 (2013).
- [12] B. Srinivasan and X.-Z. Tang, The mitigating effect of magnetic fields on Rayleigh-Taylor unstable inertial confinement fusion plasmas, *Phys. Plasmas* **20**, 056307 (2013).
- [13] C. A. Walsh, S. O'Neill, J. P. Chittenden, A. J. Crilly, B. Appelbe, D. J. Strozzi, D. Ho, H. Sio, B. Pollock, L. Divol *et al.*, Magnetized ICF implosions: Scaling of temperature and yield enhancement, *Phys. Plasmas* **29**, 042701 (2022).
- [14] J. D. Moody, B. B. Pollock, H. Sio, D. J. Strozzi, D. D.-M. Ho, C. A. Walsh, G. E. Kemp, B. Lahmann, S. O. Kucheyev, B. Koziolowski *et al.*, Increased ion temperature and neutron yield observed in magnetized indirectly driven D₂-filled capsule implosions on the national ignition facility, *Phys. Rev. Lett.* **129**, 195002 (2022).
- [15] C. A. Walsh, K. McGlinchey, J. K. Tong, B. D. Appelbe, A. Crilly, M. F. Zhang, and J. P. Chittenden, Perturbation modifications by pre-magnetisation of inertial confinement fusion implosions, *Phys. Plasmas* **26**, 022701 (2019).
- [16] C. A. Walsh, A. J. Crilly, and J. P. Chittenden, Magnetized directly-driven ICF capsules: increased instability growth from non-uniform laser drive, *Nucl. Fusion* **60**, 106006 (2020).
- [17] A. Bose, J. Peebles, C. A. Walsh, J. A. Frenje, N. V. Kabadi, P. J. Adrian, G. D. Sutcliffe, M. Gatu Johnson, C. A. Frank, J. R. Davies *et al.*, Effect of strongly magnetized electrons and ions on heat flow and symmetry of inertial fusion implosions, *Phys. Rev. Lett.* **128**, 195002 (2022).
- [18] M. R. Gomez, S. A. Slutz, A. B. Sefkow, D. B. Sinars, K. D. Hahn, S. B. Hansen, E. C. Harding, P. F. Knapp, P. F. Schmit, C. A. Jennings *et al.*, Experimental demonstration of fusion-relevant conditions in magnetized liner inertial fusion, *Phys. Rev. Lett.* **113**, 155003 (2014).
- [19] M. R. Gomez, S. A. Slutz, C. A. Jennings, D. J. Ampleford, M. R. Weis, C. E. Myers, D. A. Yager-Elorriaga, K. D. Hahn, S. B. Hansen, E. C. Harding *et al.*, Performance scaling in magnetized liner inertial fusion experiments, *Phys. Rev. Lett.* **125**, 155002 (2020).
- [20] J. R. Davies, D. H. Barnak, R. Betti, E. M. Campbell, P. Y. Chang, A. B. Sefkow, K. J. Peterson, D. B. Sinars, and M. R. Weis, Laser-driven magnetized liner inertial fusion, *Phys. Plasmas* **24**, 062701 (2017).
- [21] D. H. Barnak, J. R. Davies, R. Betti, M. J. Bonino, E. M. Campbell, V. Y. Glebov, D. R. Harding, J. P. Knauer, S. P. Regan, A. B. Sefkow *et al.*, Laser-driven magnetized liner inertial fusion on OMEGA, *Phys. Plasmas* **24**, 056310 (2017).
- [22] E. C. Hansen, D. H. Barnak, R. Betti, E. M. Campbell, P. Y. Chang, J. R. Davies, V. Y. Glebov, J. P. Knauer, J. Peebles, S. P. Regan *et al.*, Measuring implosion velocities in experiments and simulations of laser-driven cylindrical implosions on the OMEGA laser, *Plasma Phys. Controlled Fusion* **60**, 054014 (2018).

- [23] E. C. Hansen, J. R. Davies, D. H. Barnak, R. Betti, E. M. Campbell, V. Y. Glebov, J. P. Knauer, L. S. Leal, J. L. Peebles, A. B. Sefkow *et al.*, Neutron yield enhancement and suppression by magnetization in laser-driven cylindrical implosions, *Phys. Plasmas* **27**, 062703 (2020).
- [24] J. L. Peebles, J. R. Davies, D. H. Barnak, V. Y. Glebov, E. C. Hansen, P. V. Heuer, L. S. Leal, M. J. Bonino, D. R. Harding, A. B. Sefkow *et al.*, Demonstration of neutron-yield enhancement by laser preheating and magnetization of laser-driven cylindrical implosions, *Phys. Plasmas* **30**, 082703 (2023).
- [25] L. C. Jarrott, B. Bachmann, T. Ma, L. R. Benedetti, F. E. Field, E. P. Hartouni, R. Hatarik, N. Izumi, S. F. Khan, O. L. Landen *et al.*, Thermal temperature measurements of inertial fusion implosions, *Phys. Rev. Lett.* **121**, 085001 (2018).
- [26] V. Y. Glebov, T. C. Sangster, C. Stoeckl, J. P. Knauer, W. Theobald, K. L. Marshall, M. J. Shoup, T. Buczek, M. Cruz, T. Duffy *et al.*, The National Ignition Facility neutron time-of-flight system and its initial performance (invited), *Rev. Sci. Instrum.* **81**, 10D325 (2010).
- [27] L. Gao, B. F. Kraus, K. W. Hill, M. B. Schneider, A. Christopherson, B. Bachmann, M. Bitter, P. Efthimion, N. Pablant, R. Betti *et al.*, Hot spot evolution measured by high-resolution x-ray spectroscopy at the National Ignition Facility, *Phys. Rev. Lett.* **128**, 185002 (2022).
- [28] M. Gatut Johnson, J. P. Knauer, C. J. Cerjan, M. J. Eckart, G. P. Grim, E. P. Hartouni, R. Hatarik, J. D. Kilkenny, D. H. Munro, D. B. Sayre *et al.*, Indications of flow near maximum compression in layered deuterium-tritium implosions at the National Ignition Facility, *Phys. Rev. E* **94**, 021202(R) (2016).
- [29] I. Golovkin, R. Mancini, S. Louis, Y. Ochi, K. Fujita, H. Nishimura, H. Shirga, N. Miyanaga, H. Azechi, R. Butzbach *et al.*, Spectroscopic determination of dynamic plasma gradients in implosion cores, *Phys. Rev. Lett.* **88**, 045002 (2002).
- [30] S. P. Regan, J. A. Delettrez, R. Epstein, P. A. Jaanimagi, B. Yaakobi, V. A. Smalyuk, F. J. Marshall, D. D. Meyerhofer, W. Seka, D. A. Haynes *et al.*, Characterization of direct-drive-implosion core conditions on OMEGA with time-resolved Ar K-shell spectroscopy, *Phys. Plasmas* **9**, 1357 (2002).
- [31] R. Florido, R. C. Mancini, T. Nagayama, R. Tommasini, J. A. Delettrez, S. P. Regan, and B. Yaakobi, Measurements of core and compressed-shell temperature and density conditions in thick-wall target implosions at the Omega laser facility, *Phys. Rev. E* **83**, 066408 (2011).
- [32] R. Florido, R. C. Mancini, T. Nagayama, R. Tommasini, J. A. Delettrez, and S. P. Regan, Time-resolved characterization and energy balance analysis of implosion core in shock-ignition experiments at OMEGA, *Phys. Plasmas* **21**, 102709 (2014).
- [33] T. Nagayama, R. C. Mancini, R. Florido, D. Mayes, R. Tommasini, J. A. Koch, J. A. Delettrez, S. P. Regan, and V. A. Smalyuk, Direct asymmetry measurement of temperature and density spatial distributions in inertial confinement fusion plasmas from pinhole space-resolved spectra, *Phys. Plasmas* **21**, 050702 (2014).
- [34] K. R. Carpenter, R. C. Mancini, E. C. Harding, A. J. Harvey-Thompson, M. Geissel, M. R. Weis, S. B. Hansen, K. J. Peterson, and G. A. Rochau, Temperature distributions and gradients in laser-heated plasmas relevant to magnetized liner inertial fusion, *Phys. Rev. E* **102**, 023209 (2020).
- [35] K. R. Carpenter, R. C. Mancini, E. C. Harding, A. J. Harvey-Thompson, M. Geissel, M. R. Weis, S. B. Hansen, K. J. Peterson, and G. A. Rochau, Magnetic field impact on the laser heating in MagLIF, *Phys. Plasmas* **27**, 052704 (2020).
- [36] J. T. Clapp, R. C. Mancini, E. C. Harding, M. A. Schaeuble, and A. J. Harvey-Thompson, Observation and diagnostic application of Kr K-shell emission in magnetized liner inertial fusion experiments at Z, *Rev. Sci. Instrum.* **93**, 103532 (2022).
- [37] R. V. Shapovalov, G. Brent, R. Moshier, M. Shoup, R. B. Spielman, and P.-A. Gourdain, Design of 30-T pulsed magnetic field generator for magnetized high-energy-density plasma experiments, *Phys. Rev. Accel. Beams* **22**, 080401 (2019).
- [38] D. Thorn, F. Coppari, T. Döppner, M. MacDonald, S. Regan, and M. Schneider, X-ray spectrometer throughput model for (selected) flat Bragg crystal spectrometers on laser plasma facilities, *Rev. Sci. Instrum.* **89**, 10F119 (2018).
- [39] A. Ciardi, S. V. Lebedev, A. Frank, E. G. Blackman, J. P. Chittenden, C. J. Jennings, D. J. Ampleford, S. N. Bland, S. C. Bott, J. Rapley *et al.*, The evolution of magnetic tower jets in the laboratory, *Phys. Plasmas* **14**, 056501 (2007).
- [40] J. Chittenden, S. Lebedev, C. Jennings, S. Bland, and A. Ciardi, X-ray generation mechanisms in three-dimensional simulations of wire array Z-pinch, *Plasma Phys. Controlled Fusion* **46**, B457 (2004).
- [41] C. A. Walsh, J. P. Chittenden, K. McGlinchey, N. P. L. Niasse, and B. D. Appelbe, Self-generated magnetic fields in the stagnation phase of indirect-drive implosions on the National Ignition Facility, *Phys. Rev. Lett.* **118**, 155001 (2017).
- [42] G. Pérez-Callejo, M. Bailly-Grandvaux, R. Florido, C. A. Walsh, M. A. Gigosos, F. N. Beg, C. McGuffey, R. C. Mancini, F. Suzuki-Vidal, C. Vlachos *et al.*, X-ray imaging and radiation transport effects on cylindrical implosions, *Rev. Sci. Instrum.* **93**, 113542 (2022).
- [43] J. R. Davies, D. H. Barnak, R. Betti, E. M. Campbell, V. Y. Glebov, E. C. Hansen, J. P. Knauer, J. L. Peebles, and A. B. Sefkow, Inferring fuel areal density from secondary neutron yields in laser-driven magnetized liner inertial fusion, *Phys. Plasmas* **26**, 022706 (2019).
- [44] I. V. Igumenshchev, D. T. Michel, R. C. Shah, E. M. Campbell, R. Epstein, C. J. Forrest, V. Y. Glebov, V. N. Goncharov, J. P. Knauer, F. J. Marshall *et al.*, Three-dimensional hydrodynamic simulations of OMEGA implosions, *Phys. Plasmas* **24**, 056307 (2017).
- [45] R. Florido, R. Rodríguez, J. M. Gil, J. G. Rubiano, P. Martel, E. Mínguez, and R. C. Mancini, Modeling of population kinetics of plasmas that are not in local thermodynamic equilibrium, using a versatile collisional-radiative model based on analytical rates, *Phys. Rev. E* **80**, 056402 (2009).
- [46] M. A. Gigosos, S. Djurović, I. Savić, D. González-Herrero, Z. Mijatović, and R. Kobilarov, Stark broadening of lines from transition between states $n = 3$ to $n = 2$ in neutral helium. An experimental and computer-simulation study, *Astron. Astrophys.* **561**, A135 (2014).
- [47] M.-A. Schaeuble, T. Nagayama, J. E. Bailey, M. A. Gigosos, R. Florido, S. Blouin, T. A. Gomez, B. Dunlap, M. H. Montgomery, and D. E. Winget, Measuring He I Stark line shapes in the laboratory to examine differences in photometric and spectroscopic DB white dwarf masses, *Astrophys. J.* **940**, 181 (2022).
- [48] H. Griem, *Spectral Line Broadening by Plasmas* (Elsevier, Amsterdam, 1974).

- [49] M. A. Gigosos, Stark broadening models for plasma diagnostics, *J. Phys. D: Appl. Phys.* **47**, 343001 (2014).
- [50] B. A. Hammel, C. J. Keane, M. D. Cable, D. R. Kania, J. D. Kilkenny, R. W. Lee, and R. Pasha, X-ray spectroscopic measurements of high densities and temperatures from indirectly driven inertial confinement fusion capsules, *Phys. Rev. Lett.* **70**, 1263 (1993).
- [51] J. E. Bailey, G. A. Chandler, S. A. Slutz, I. Golovkin, P. W. Lake, J. J. MacFarlane, R. C. Mancini, T. J. Burris-Mog, G. Cooper, R. J. Leeper *et al.*, Hot dense capsule-implosion cores produced by Z-pinch dynamic Hohlraum radiation, *Phys. Rev. Lett.* **92**, 085002 (2004).
- [52] H. R. Griem, *Principles of Plasma Spectroscopy* (Cambridge University Press, Cambridge, UK, 1997).
- [53] M. Hohenberger, P. Y. Chang, G. Fiksel, J. P. Knauer, R. Betti, F. J. Marshall, D. D. Meyerhofer, F. H. Séguin, and R. D. Petrasso, Inertial confinement fusion implosions with imposed magnetic field compression using the OMEGA Laser, *Phys. Plasmas* **19**, 056306 (2012).
- [54] G. Pérez-Callejo, C. Vlachos, C. A. Walsh, R. Florido, M. Bailly-Grandvaux, X. Vaisseau, F. Suzuki-Vidal, C. McGuffey, F. N. Beg, P. Bradford *et al.*, Cylindrical implosion platform for the study of highly magnetized plasmas at Laser MegaJoule, *Phys. Rev. E* **106**, 035206 (2022).